



This is the peer reviewed version of the following article:

Zhang, K., Marszalek, T., Wucher, P., Wang, Z., Veith, L., Lu, H., et al. (2018). Crystallization Control of Organic Semiconductors during Meniscus-Guided Coating by Blending with Polymer Binder. *Advanced Functional Materials*, 28(50): 1805594. doi:10.1002/adfm.201805594.

, which has been published in final form at: [10.1002/adfm.201805594](https://doi.org/10.1002/adfm.201805594)

Crystallization Control of Organic Semiconductors during Meniscus-Guided Coating by Blending with Polymer Binder

Ke Zhang, Tomasz Marszalek, Philipp Wucher, Zuyuan Wang, Lothar Veith, Hao Lu, Hans-Joachim Räder, Pierre M. Beaujuge, Paul W. M. Blom, and Wojciech Pisula*

Crystallization Control of Organic Semiconductors during Meniscus-Guided Coating by**Blending with Polymer Binder**

Ke Zhang,^a Tomasz Marszalek,^{a,b} Philipp Wucher,^c Zuyuan Wang,^a Lothar Veith,^a Hao Lu,^a Hans-Joachim Räder,^a Pierre M. Beaujuge,^c Paul W. M. Blom,^a and Wojciech Pisula^{a,b}*

^a Max Planck Institute for Polymer Research, Ackermannweg 10, 55128 Mainz, Germany

^b Department of Molecular Physics, Faculty of Chemistry, Lodz University of Technology, Zeromskiego 116, 90-924 Lodz, Poland

^c Physical Sciences and Engineering Division, Solar & Photovoltaic Engineering Research Center (SPERC), King Abdullah University of Science and Technology (KAUST), Thuwal 23955-6900, Saudi Arabia

*To whom correspondence should be addressed.

Email: pisula@mpip-mainz.mpg.de

Keywords: dip-coating, semiconductor-insulator blend, crystallization control, morphology, organic field-effect transistor

Abstract

Small molecule organic semiconductors (OSCs) suffer from their uncontrolled nucleation and growth during solution processing limiting their functionality in electronic devices. In this work, we present a new method based on dip-coating a blend consisting of OSC and insulating polymer to control the crystallization of the active film for organic field-effect transistors. A small fraction of amorphous poly(methyl methacrylate) (PMMA) efficiently improves the crystallization of dip-coated small molecule OSCs, α,ω -dihexylquaterthiophene (DH4T) and diketopyrrolopyrrole-sexithiophene (DPP6T). The maximum charge carrier mobilities of dip-coated OSC:PMMA films are significantly higher than drop-cast blend ones and comparable with OSC single crystals. The high charge carrier mobility originates from a continuous alignment of the crystalline films and stratified OSC and PMMA layers. The improved crystallization is attributed to two mechanisms: firstly, the polymer binder leads to a viscosity gradient at the meniscus during dip-coating, facilitating the draw of solute and thus mass transport. Secondly, the polymer binder solidifies at the bottom layer, reducing the nucleation barrier height of small molecule OSC. Our findings demonstrate that a small fraction of a polymer binder during dip-coating efficiently balances the mass transport during

solution processing and improves the crystallization as well as the electronic properties of small molecule OSC films.

Introduction

Organic field-effect transistors (OFETs) have attracted tremendous attention owing to their large-scale solution-based processing and mechanical flexibility.^[1,2] Molecular engineering of novel conjugated small molecules and polymers as organic semiconductors (OSCs) improved their charge carrier mobilities to above $10 \text{ cm}^2 \text{ V}^{-1} \text{ s}^{-1}$.^[3,4] However, processing of small molecule OSC into continuous crystalline thin films remains a challenge due to the low viscosity and dewetting propensity of their solutions.^[5] Several methodologies have been developed to control the film morphology and optimize the molecular organization. The methods include solvent vapor annealing,^[6] structural template pattern,^[7] addition of nucleating agents,^[8] flow-induced crystallization,^[5,9] and insulator polymer blending.^[10,11]

Blending small molecule OSC with insulating polymers has been demonstrated as an effective way to fabricate high performance OFETs with high reproducibility,^[10-12] including OSCs such as rubrene,^[13] TIPS-pentacene,^[14] dioctyl benzothieno benzothiophene (C8-BTBT),^[12] and difluoro bis(triethylsilylethynyl) anthradithiophene (diF-TES-ADT).^[15,16] In the case of off-center spin-coating, a vertical phase-separated morphology between C8-BTBT and polystyrene (PS) resulted in a high field-effect mobility of even $20 \text{ cm}^2 \text{ V}^{-1} \text{ s}^{-1}$.^[12] Roll-to-roll blade-cast films of diF-TES-ADT and PS blends exhibited also an excellent charge carrier mobility as high as $6.7 \text{ cm}^2 \text{ V}^{-1} \text{ s}^{-1}$ due to a precise control over the phase separation and crystallization of the organic semiconductor.^[15] The vertical phase separation contributes to the formation of continuous stratified layers of highly crystalline small molecule OSC which grow into interconnected crystalline domains without sacrificing the intrinsic mobility of OSC.^[16] However, the understanding of the correlation between the casting conditions and the resulted morphology in terms of the crystallization mechanism of small molecule OSC in the blend is still incomplete.

Dip-coating is an efficient technique to deposit OSC thin films with well controlled morphologies.^[17-19] In dip-coating, the film formation is initiated at the solution-substrate contact line and dominated by the solvent evaporation and substrate withdrawal.^[20] It is challenging to dip-coat small molecule OSC into large-area, uniform, and continuous crystalline films due to their low film-forming ability.^[21] Therefore, dip-coating of OSC and polymer blends may mitigate the challenges associated to solution processing of small conjugated molecules since the polymer binder is expected to improve the film-forming ability. Furthermore, a careful control of the dip-coating conditions, such as the withdrawal speed, solution concentration, and solvent evaporation rate, allows a systematic investigation of the influence of the polymer binder on the crystallization kinetics of the small molecule OSC.

In this work, we have investigated the film formation of dip-coated blends consisting of small conjugated molecule OSCs, α,ω -dihexylquaterthiophene (DH4T) or diketopyrrolopyrrole-sexithiophene (DPP6T), and an amorphous insulator polymer binder, poly(methyl methacrylate) (PMMA). Under optimized conditions aligned crystalline films of DH4T:PMMA and DPP6T:PMMA were obtained. To understand the influence of the polymer binder on the crystallization of the small molecule OSC, a systematical study was performed. Thereby, the effects of the dip-coating speed, weight fraction (wt%) and molecular weight (MW) of the polymer binder on the film morphology, molecular organization, and charge carrier transport in field-effect transistors were investigated. It was found that during the dip-coating of the blends, the polymer binder results in a viscosity gradient at the meniscus drawing more small molecule OSC from solution for mass deposition. The polymer binder solidifies at the bottom layer and decreases the nucleation barrier height of the small molecule OSC. By adjusting the balance between mass transport and crystal growth, the crystal morphology of dip-coated DH4T:PMMA improves from dendritic crystals to long-range aligned crystalline films. At optimized wt%, MW and dip-coating speed, high charge

carrier mobilities of dip-coated DH4T:PMMA and DPP6T:PMMA films were obtained, 6 and 2.5 times higher than those of drop-cast DH4T:PMMA and DPP6T:PMMA ones, respectively. The values are comparable with those of vacuum sublimated films and single crystals.^[22-24] This methodology can be used to well control and improve the crystallization behavior of small molecule OSC for electronic devices, allowing a better understanding about the role of polymer binder on assisting the crystallization of small molecule OSC.

Results and discussion

Meniscus-guided coating is an efficient approach for deposition of OSCs films.^[9,25] The schematic in **Figure 1a** illustrates the dip-coating process involving a concave solution meniscus during the vertical withdrawal of a substrate from solution. The molecular structures of DH4T, DPP6T, and insulator polymer PMMA are presented in Figure 1b. Three different MWs of PMMA, 2 kDa, 100 kDa, and 2480 kDa were studied. The DH4T:PMMA_(100 kDa, 10%) blend was dip-coated from a 3 mg/mL CHCl₃ solution at a speed of 5 μm/s on a Si/SiO₂ substrate treated by oxygen plasma. In this case, CHCl₃ was selected as the solvent because of its good solubility of small molecule OSC and relatively low boiling point of 61 °C with high partial pressure leading to a high evaporate rate at room temperature.^[26, 27] The silicon wafer was treated by oxygen plasma to achieve high surface energy of the substrate and to ensure wettability that supports the film formation during solution processing.^[28] Polarized optical microscopy (POM) image in Figure 1c displays aligned crystalline ribbons of the DH4T:PMMA_(100 kDa, 10%) film. These structures are highly birefringent and optically anisotropic indicating high order and long-range macroscopic orientation of DH4T molecules. In contrast, when dip-coating pristine DH4T only few aggregates were formed at the edge of the silicon substrate but no nucleation on the SiO₂ surface occurred, as shown in Figure S1. Bottom gate and top contact (BGTC) transistors based on the dip-coated DH4T:PMMA_(100 kDa, 10%) film were fabricated with the channel parallel to the alignment of the crystalline ribbons.

Typical transfer and output curves are shown in Figure 1d. A hole mobility of $0.05 \text{ cm}^2 \text{ V}^{-1} \text{ s}^{-1}$ is obtained with an on/off ratio of around 10^6 and a threshold voltage of -17 V .

To understand the effect of PMMA on the crystallization kinetics of DH4T during dip-coating, systematic studies were performed with the focus on the role of wt% and MW of PMMA. As shown in **Figures 2a** and S2, POM and atomic forced microscopy (AFM) images exhibit the morphology of DH4T:PMMA_(100 kDa) for the dip-coating speeds of $5 \mu\text{m/s}$, $10 \mu\text{m/s}$ and $20 \mu\text{m/s}$ and different wt% of PMMA from 2 wt%, to 5 wt% and 10 wt%. During dip-coating, solvent evaporation and substrate withdraw lead to solute supersaturation at the meniscus, inducing nucleation and crystal growth at the contact line.^[9] By decreasing the dip-coating speed of the DH4T:PMMA blend, dendritic crystals between the substrate withdrawal and solvent evaporation, leading to an insufficient mass transport for gradually change into long-range aligned crystalline ribbons and the film thickness increases continuously from 20 nm to 250 nm (Figure S2a). The dendritic crystals originate from mismatch the crystal growth. Interestingly, blending of PMMA can enhance the mass transport and improve the crystal growth of DH4T. In this way, the formation of dendritic crystals is inhibited and crystalline ribbons with high coverage are grown. The MW of PMMA was varied from 2 kDa to 100 kDa and 2480 kDa for DH4T:PMMA_(10%) to understand the effect of MW of PMMA on the growth of DH4T. Low-MW PMMA_(2 kDa) leads to dendritic crystals at a high dip-coating speed of $20 \mu\text{m/s}$ and to crystalline ribbons with a low coverage at $5 \mu\text{m/s}$ (Figure 2b). The high-MW PMMA_(2480 kDa) favors the alignment of the dendritic crystals at $20 \mu\text{m/s}$ and significantly enhances the coverage density of crystalline ribbons at $5 \mu\text{m/s}$. The morphology characterization proves that blending of a small wt% of the polymer binder can efficiently improve the crystallization of small molecule OSC during dip-coating. However, this does not mean that higher wt% or Mw of PMMA can further improve the morphology of dip-coated DH4T:PMMA. For instance, the dip-coated DH4T:PMMA_(2480 kDa, 50%) films obtained at $5 \mu\text{m/s}$ exhibit a stick-slip morphology (Figure S3) which inhibits the charge carrier transport.^[29]

Therefore, a high quality crystalline morphology requires an optimized PMMA ratio at appropriate coating parameters.

Bottom-gate and top-contact (BGTC) transistors based on dip-coated DH4T:PMMA films were fabricated, in which the crystalline ribbons were aligned along the channel. The mobility is calculated based on only the capacitance of only the 300 nm SiO₂ dielectric (due to the low ratio of PMMA) to simplify the comparison of the charge carrier transport. As shown in Figure 2c, the mobilities of dip-coated DH4T:PMMA_(100 kDa) films increase with the decrease of the dip-coating speed. For the same dip-coating speed, high-wt% PMMA leads to a higher charge carrier mobility (Figure 2c). In the case of 5 μm/s, DH4T blending with 10 wt% PMMA_(100 kDa) exhibits an average mobility of 0.05 cm² V⁻¹ s⁻¹ which is 2 and 6 times higher than that with 5 wt% and 2 wt% PMMA, respectively (transfer and output curves are shown in Figures S4-6). Concerning the MW of PMMA, high-MW PMMA results in more homogeneous morphologies and thereby higher charge carrier mobilities (Figures 2d and S6-8). A maximum mobility of 0.1 cm² V⁻¹ s⁻¹ is obtained for the dip-coated DH4T:PMMA_(2480 kDa, 10%) film at 5 μm/s which is on par with the highest values for DH4T single crystals and vacuum sublimated films.^[22,23] However, the device performance of dip-coated DH4T:PMMA films depends on their crystalline morphology. A high void area and low degree of alignment lead to a low charge carrier mobility.

For spin-coated and drop-cast film, the influence of a small fraction of PMMA on the DH4T crystallization is minor. Discontinuous aggregates are formed after spin-coating both pristine DH4T and DH4T:PMMA_(2480 kDa, 10%), as shown in Figure S8. After drop-casting, pristine DH4T grows into randomly distributed crystal flakes, while the drop-cast DH4T:PMMA_(2480 kDa, 10%) film reveals mainly flake-like crystals and few dendritic one (Figure S9). These results indicate that PMMA weakly influences the crystallization of DH4T during spin-coating and drop-casting. The charge carrier mobilities for drop-cast pristine DH4T and

DH4T:PMMA_(2480 kDa, 10%) films are $0.015 \text{ cm}^2 \text{ V}^{-1} \text{ s}^{-1}$ and $0.013 \text{ cm}^2 \text{ V}^{-1} \text{ s}^{-1}$, respectively (Figure S10).

To understand the origin of the improved crystallization induced by blending PMMA during dip-coating of DH4T, the meniscus angle and solution viscosity were studied. As shown in **Figures 3a** and S11, the meniscus angle for the dilute PMMA/CHCl₃ solution (less than 3 mg/mL) is around 32-34°, which is independent on wt% and MW of PMMA, and corresponds to the meniscus angle of CHCl₃. In addition, the meniscus angle of PMMA/CHCl₃ solution is fixed and remains also unchanged at different dip-coating speeds. This stable meniscus shape results from the low surface tension of CHCl₃ (26.7 mN/m).^[30] This proves that a small fraction of PMMA does not influence the dip-coating meniscus angle of the CHCl₃ solution. The dynamic viscosity of a solution containing small conjugated molecules mainly depends on the solvent viscosity in contrast to a polymer solution.^[31] In our case, we assumed that only PMMA influence the viscosity of solution, since PMMA chains entangle at the increased concentration and result in stronger interchain forces leading to a high viscosity.^[32] Thereby, the viscosity of the DH4T/CHCl₃ solution is a constant and identical to that of CHCl₃ ($\eta_0 = 0.61 \text{ cP}$), while the viscosity of the DH4T:PMMA/CHCl₃ solution is attributed to the wt% and MW of PMMA. As shown in Figure 3b, the viscosity of the dilute PMMA/CHCl₃ solution increases with wt% and MW of PMMA. At a concentration of $c_{\text{PMMA}} = 0.3 \text{ mg/mL}$ (corresponding to the 10 wt% PMMA in 3 mg/mL DH4T:PMMA/CHCl₃), the viscosity of the bulk solution (η_{bulk}) of PMMA_(2480 kDa)/CHCl₃ is around 0.68 cP, only slightly higher than η_0 (Table S1). However, the viscosity at the meniscus during dip-coating is expected to be higher due to the increased solution concentration caused by solvent evaporation. The viscosity of defined DH4T/CHCl₃ and defined DH4T:PMMA_(2480 kDa, 10%)/CHCl₃ at the meniscus is estimated by COMSOL (Figure S12). As shown in Figure 3c, a viscosity gradient of defined DH4T:PMMA_(2480 kDa, 10%)/CHCl₃ is formed at the meniscus due to blending of PMMA in contrast to the constant viscosity of defined DH4T/CHCl₃. The calculated result exhibits an

obvious viscosity-gradient at the meniscus, and an even higher viscosity is expected at the solution-substrate contact line in reality. As a consequence, the thickness of dip-coated PMMA_(2480 kDa) is higher than those for PMMA_(100 kDa) and PMMA_(2 kDa), as shown in Figure 3d. It demonstrates that viscosity-gradient at the meniscus contributes to the increased mass transport for the film deposition. Therefore, the viscosity-gradient at the meniscus plays a crucial role on improving the crystallization of DH4T.

To reveal the phase separation and distribution of the two components in the dip-coated DH4T:PMMA film, time-of-flight secondary ion mass spectrometry (ToF-SIMS) and X-ray photoelectron spectroscopy (XPS) analysis were performed. Depth profiles in the negative secondary ion polarity of the DH4T:PMMA_(2480 kDa, 10%) film were acquired in the ToF-SIMS dual-beam depth profiling mode (**Figure 4a,b**). For the crystalline area (Figure 4a, highlighted circle in the inset optical image), the depth profile shows in the sputter time from 0 s to 60 s a constant high intensity of DH4T-specific ions (S^- , C_6HS^-) and low intensity of PMMA-specific ones (CH_3O^- , $C_4H_5O_2^-$). After this sputter time, the DH4T signals decrease, while the PMMA signals increase. This indicates a vertical phase separation in the dip-coated DH4T:PMMA film with a top DH4T layer and bottom PMMA layer. The vertical distribution between DH4T and PMMA is induced by the difference in surface energy of the compounds. As shown in Figure S13, the contact angle of water on PMMA ($57\pm 1^\circ$) is lower than on DH4T ($91\pm 2^\circ$) indicating a lower surface energy of DH4T. Therefore, in dip-coated blend films DH4T preferentially accumulates at the top film surface to reduce the overall energy. The average thickness of the bottom PMMA layer for dip-coated DH4T:PMMA_(2480 kDa, 10%) is around 23 nm (Figure S14). In the non-crystalline area (highlighted triangle in the inset optical image of Figure 4b), PMMA (CH_3O^- , $C_4H_5O_2^-$) signals decrease from the beginning within the first 20 s indicating a thin PMMA layer, while no DH4T (S^- , C_6HS^-) were detected (Figure 4b). The lateral signal distribution of compound-specific positive ions on the film top surface exposes the complementary distribution of DH4T ($C_{28}H_{35}S_4^+$, Figure 4c) and PMMA

($C_2H_3O_2^+$, Figure 4d). XPS analysis further identifies the chemical composition of the film surface in the crystalline area. The theoretical carbon/sulfur ratio for pristine DH4T is 7, while the carbon/sulfur ratio of the top surface of dip-coated DH4T:PMMA films as extracted from the XPS analysis is higher than 7. For instance, the DH4T:PMMA_(10 wt%) films coated at 5 $\mu\text{m/s}$ reveal a carbon/sulfur ratio between 9 and 15 for different MWs of PMMA (Figure S15 and S16). Since XPS is surface sensitive by probing the top 8 nm of the film, the high carbon/sulfur ratio and large variation indicate a low concentration of PMMA at the top surface of the DH4T crystals.^[35] This is in agreement with the ToF-SIMS depth profile in Figure 5a. ToF-SIMS and XPS results reveal that the dip-coated DH4T:PMMA films consist of top crystalline DH4T ribbons and a continuous bottom PMMA layer resulting from the vertical phase separation (Figure 4e).

The schematic illustrations of the dip-coating process for PMMA, DH4T, and DH4T:PMMA (optimized wt% and MW of PMMA) are shown in **Figure 5**. In the evaporation regime, the liquid flow is dominated by the evaporation-driven capillary flow leading to the film growth at the solution-substrate contact line.^[9] Dip-coating of PMMA from $CHCl_3$ yields a continuous film (Figure 5a). Since the concentration of PMMA increases with solvent evaporation, a higher viscosity occurs at the dip-coating meniscus. The entanglement of polymer coils results in strong interchain forces, contributing to the film formation.^[32] In contrast, pure DH4T poorly nucleates since the insufficient mass transport of solute inhibits the nucleation of DH4T crystals (Figures 5b and S1). As for dip-coating of DH4T:PMMA, a viscosity gradient at the meniscus is established due to the blending of PMMA (Figure 5c). The increased viscosity draws more DH4T from solution to the solution-substrate contact line. Further solvent evaporation results in supersaturation at the meniscus near the contact line. The entangled PMMA chains are more prone to solidify on the substrate surface than DH4T. As consequence, PMMA firstly solidifies at the contact line and forms a continuous layer on the substrate. The solidified bottom PMMA layer reduces the barrier height of nucleation only

on a few nucleation points and induces large-scale growth of DH4T by suppressing random creation of spontaneous nucleation.^[36] The MW of PMMA plays also an important role on the DH4T crystallization. High-MW PMMA shows higher interchain forces stronger supporting the formation of aligned DH4T crystal ribbons, while low-MW PMMA leads only to dendritic crystals of DH4T.

To understand the effect of the polymer binder on the DH4T molecular organization, the dip-coated DH4T:PMMA_(2480 kDa, 10%) film was further examined via grazing incidence wide-angle X-ray scattering (GIWAXS) and selected area electron diffraction (SAED). The corresponding GIWAXS and SAED patterns are shown in **Figure 6** and the unit cell parameters are listed in Table S2. For drop-cast pristine DH4T film, the GIWAXS pattern exhibits a notably high number of reflections, implying a pronounced crystallinity (Figure 6a). The main meridional reflection at $q_z = 0.22 \text{ \AA}^{-1}$ for $q_{xy} = 0 \text{ \AA}^{-1}$ is assigned to an interlayer distance of 2.84 nm. The wide-angle equatorial scattering intensity at $q_z = 0 \text{ \AA}^{-1}$ for $q_{xy} = 1.61 \text{ \AA}^{-1}$ is related to a π -stacking distance of 0.39 nm. The reflections for the drop-cast DH4T:PMMA_(2480 kDa, 10%) film are located on identical positions, but are smeared over the azimuthal direction of the pattern (Figure 6b) characteristic for randomly oriented crystals on the surface. In contrast, the dip-coated DH4T:PMMA_(2480 kDa, 10%) film shows a sufficient scattering intensity indicating still a high crystallinity of oriented DH4T (Figure 6c). The interlayer distance and π -stacking distance of dip-coated DH4T:PMMA film are 2.85 nm and 0.39 nm, respectively, verifying an identical molecular organization as found for drop-cast DH4T (schematic illustration in Figure S17). Figure 6d-f presents the highlighted diffraction peaks in the SAED patterns for indexing the unit cell. Based on the GIWAXS and [001] zone electron diffraction patterns, a *monoclinic* unit cell of $a_0=5.93 \text{ \AA}$, $b_0=7.88 \text{ \AA}$, and $c_0=28.42 \text{ \AA}$ for drop-cast DH4T is derived. These parameters are identical to the reported DH4T unit cell of thermally evaporated films.^[37] The structural analysis revealed nearly unchanged monoclinic parameters for the drop-cast DH4T:PMMA film with $a_1=5.88 \text{ \AA}$, $b_1=7.70 \text{ \AA}$,

$c_1=28.24$, and for dip-coated DH4T:PMMA with $a_2=5.81$ Å, $b_2=7.70$ Å, $c_2=28.53$. This indicates that no polymorph of DH4T is formed in the dip-coated DH4T:PMMA film, different with the case of TIPS-pentacene blended with P3HT during slow solution crystallization.^[38] Therefore it can be concluded that amorphous PMMA efficiently assists during dip-coating the crystallization of small molecule OSC with high crystallinity without influencing the unit cell parameters.

To prove the general character of the polymer binder on the crystallization of small molecule OSC during dip-coating, DPP6T was additionally chosen as model compound since its transistor performance suffers from the uncontrolled crystal growth during drop-casting.^[24] For pristine DPP6T, only discontinuous small crystals were obtained by dip-coating at 3 mg/mL from CHCl_3 due to the poor film-formation ability (Figure S18). Varying dip-coating speed did not improve the film morphology. For dip-coating DPP6T:PMMA, the fraction (2 wt%, 5 wt%, and 10 wt%) and MW (2 kDa, 100 kDa, and 2480 kDa) of PMMA were varied (**Figure 7**). As shown in Figure 7a, blending 100 kDa PMMA induces an alignment of the DPP6T crystals, while a higher wt% of PMMA and slower dip-coating speed lead to larger crystal domains. The increase in MW of PMMA improves the film homogeneity (Figure 7b). However, few cracks and wrinkles appear in the high-MW blend when the dip-coating speed decreases to 10 $\mu\text{m/s}$ and 5 $\mu\text{m/s}$ due to stress induced during film drying (Figures 7b and S19).^[20]

The charge carrier mobility of dip-coated DPP6T:PMMA films with crystals aligned along transistor channel is summarized in Figure 7c,d, and the transfer and output curves are shown in Figures S20-24. The mobility of DPP6T:PMMA is calculated based on the capacitance of 300 nm SiO_2 to simply the comparison of the charge carrier transport, since the change in capacitance due to the additional thin bottom PMMA layer is negligible (Figure S25). The mobility of the DPP6T:PMMA films increases with wt% and MW of PMMA (Figure 7c,d), owing to its homogenous morphology, which is in agreement with the trend observed for the

dip-coated DH4T:PMMA blend. In contrast to the DH4T:PMMA blend, the highest mobility of $0.55 \text{ cm}^2 \text{ V}^{-1} \text{ s}^{-1}$ of the DPP6T:PMMA_(2480 kDa, 10%) blend is found for the highest dip-coating speed of $20 \text{ } \mu\text{m/s}$. This suggests that the dip-coating speed need to be carefully optimized for each special small molecule OSC due to their different self-assembly ability. For spin-coated DPP6T and DPP6T:PMMA_(2480 kDa, 10%), mobilities of around $0.05 \text{ cm}^2 \text{ V}^{-1} \text{ s}^{-1}$ and $0.02 \text{ cm}^2 \text{ V}^{-1} \text{ s}^{-1}$, respectively, were determined. These low values arise from the low film crystallinity (Figures S25 and S26). The low mobility of $0.005 \text{ cm}^2 \text{ V}^{-1} \text{ s}^{-1}$ of drop-cast DPP6T films is caused by the rough interface between semiconductor and dielectric (Figure S25 and S27).^[24] Drop-cast DPP6T:PMMA_(2480 kDa, 10%) exhibits spherulite crystals and leads to a mobility of $0.2 \text{ cm}^2 \text{ V}^{-1} \text{ s}^{-1}$ which is lower than that of dip-coated DPP6T:PMMA_(2480 kDa, 10%) since grain boundaries between spherulite crystals of the drop-cast DPP6T:PMMA film inhibit the charge transport. These results prove that a small fraction of the polymer binder also significantly improve the crystallization and charge carrier transport in dip-coated DPP6T:PMMA films.

Conclusion

This work demonstrates that using a minor amount of an insulating amorphous polymer binder efficiently improves the crystallization of small molecule OSC during dip-coating. A continuous alignment of the crystalline films with stratified OSC/polymer layers was obtained at optimizing conditions, contributing to an enhanced charge carrier transport in transistors. It gives an insight into the superiority of meniscus-guided coating on enlarging the role of polymer binder to improve the crystallization of OSC. Maximum mobilities for dip-coated DH4T:PMMA and DPP6T:PMMA are 6 times and 2.5 times higher than those of corresponding drop-cast ones, and are comparable with those of vacuum sublimated films and single crystals. Our work provides an understanding on the crystallization mechanism of small molecule OSC in the presence of a polymer binder during meniscus-guided coating for applications in field-effect transistors. We anticipate that this efficient and convenient methodology is broadly applicable to various soluble crystalline organic semiconductors,

since misaligned crystalline grains and morphological defects are commonly encountered problems during the coating processes.

Experimental Section

Material and Synthesis: DH4T was purchased from Syncom without further purification. PMMA was purchased from Sigma Aldrich. The synthesis details of DPP6T are described in the Supporting Information.

Characterization: The film morphology was characterized by a Leica POM and a Digital Instruments Nanoscope IIIa AFM in tapping mode. Contact angle measurements were performed with a contact angle meter, Data Physics, OCA35. The solution viscosities were obtained by a standard Ostwald capillary viscometer. XPS measurements were conducted on a Kratos Axis Ultra^{DLD} spectrometer (Kratos, Manchester, England). GIWAXS measurements were performed by means of a solid anode X-ray tube (Siemens Kristalloflex X-ray source, copper anode X-ray tube operated at 35 kV and 40 mA), Osmic confocal MaxFlux optics, X-ray beam with pinhole collimation and a MAR345 image plate detector. A transmission electron microscopy (FEI Tecnai F20) and corresponding SAED were used to gain structural information. A Keithley 4200-SCS was used for all standard electronic measurements in glove-box under nitrogen atmosphere. ToF-SIMS was performed using a TOF.SIMS⁵ NCS instrument (IONTOF, Münster, Germany) with 30 keV Bi₃ primary ions and 5 keV Ar₁₅₀₀ cluster ions for sputtering at 45° angle. Profiling was facilitated in the dual beam depth profiling mode.

Organic Semiconductor Deposition and Device Fabrication: Silicon substrates with a 300 nm thick SiO₂ layer were treated by oxygen plasma for 3 min. Dip-coating of the pure compounds and blends was performed from CHCl₃ at concentrations of 3 mg/mL for DH4T and DPP6T. The same solutions were used for spin-coating at 2000 rpm for 60s. During drop-casting, the solvent evaporation took place under a glass petri for 20-30 min, the optimized drop-casting conditions were obtained by controlling the evaporation time. A bottom-gate top-contact

configuration was employed for OFET devices. Heavily doped n-type Si wafers were used as gate electrode and a 300 nm thick SiO₂ layer (capacitance of 11 nF cm⁻²) was adopted as a gate dielectric layer. Source and drain electrodes were deposited at a thickness of 50 nm by gold evaporation. The transistor channel length and width were 1000 μm and 25 μm, respectively. The average mobilities for all organic semiconductors were calculated from three to seven transistors based on the saturated regime. Since the average thickness of the bottom PMMA layer for dip-coated OSC:PMMA film is less than 40 nm, the corresponding capacitance (including 300nm SiO₂) is around 10-11 nF cm⁻². To simplify the comparison of the charge carrier transport, the mobilities of all devices were calculated based on the capacitance of 11 nF cm⁻². Though the simplification of mobility calculation leads to a slightly underestimation, there is no influence on key conclusions of this work.

Supporting Information

The supporting information is available from the Wiley Online Library or from the author.

Acknowledgement

The authors declare no competing financial interest. K. Zhang thanks the China Scholarship Council (CSC) for financial support. T. Marszalek acknowledges the Foundation for Polish Science co-financed by the European Union under the European Regional Development Fund (First TEAM/2017-3/26). W. Pisula acknowledges the National Science Centre, Poland, through the grant UMO-2015/18/E/ST3/00322. P. M. Beaujuge acknowledges concurrent support from the King Abdullah University of Science and Technology (KAUST) Office of Sponsored Research (OSR) under Award No. CRG_R2_13_BEAU_KAUST_1 and under Baseline Research Funding. P. Wucher thanks the KAUST ACL for technical support in the mass spectrometry analyses. Z. Wang acknowledges the support by ERC (SmartPhon No. 694977).

Conflict of Interest

The authors declare no conflict of interest.

Reference

- [1] Y. Yao, H. Dong, W. Hu, *Adv. Mater.* **2016**, 28, 4513.
- [2] S.J. Benight, C. Wang, J.B.H. Tok, Z. Bao, *Prog. Polym. Sci.* **2013**, 38, 1961.
- [3] J.H. Dou, Y.Q. Zheng, Z.F. Yao, T. Lei, X. Shen, X.Y. Luo, Z.A. Yu, S.D. Zhang, G. Han, Z. Wang, Y. Yi, J.Y. Wang, J. Pei, *Adv. Mater.* **2015**, 27, 8051.

- [4] H. Siringhaus, *Adv. Mater.* **2014**, *26*, 1319.
- [5] Y. Diao, L. Shaw, Z. Bao, S.C.B. Mannsfeld, *Energy Environ. Sci.* **2014**, *7*, 2145.
- [6] C. Liu, T. Minari, Y. Li, A. Kumatani, M.V. Lee, S.H. Athena Pan, K. Takimiya, K. Tsukagoshi, *J. Mater. Chem.* **2012**, *22*, 8462.
- [7] Y. Diao, B.C. Tee, G. Giri, J. Xu, H. Kim do, H.A. Becerril, R.M. Stoltenberg, T.H. Lee, G. Xue, S.C. Mannsfeld, Z. Bao, *Nat. Mater.* **2013**, *12*, 665.
- [8] N.D. Treat, J.A. Nekuda Malik, O. Reid, L. Yu, C.G. Shuttle, G. Rumbles, C.J. Hawker, M.L. Chabinyc, P. Smith, N. Stingelin, *Nat. Mater.* **2013**, *12*, 628.
- [9] G. Qu, J.J. Kwok, Y. Diao, *Acc. Chem. Res.* **2016**, *49*, 2756.
- [10] W. Lee, Y. Park, *Polymers* **2014**, *6*, 1057.
- [11] J. Smith, R. Hamilton, I. McCulloch, N. Stingelin-Stutzmann, M. Heeney, D.D.C. Bradley, T.D. Anthopoulos, *J. Mater. Chem.* **2010**, *20*, 2562.
- [12] Y. Yuan, G. Giri, A.L. Ayzner, A.P. Zoombelt, S.C. Mannsfeld, J. Chen, D. Nordlund, M.F. Toney, J. Huang, Z. Bao, *Nat. Commun.* **2014**, *5*, 3005.
- [13] P.S. Jo, D.T. Duong, J. Park, R. Sinclair, A. Salleo, *Chem. Mater.* **2015**, *27*, 3979.
- [14] B.K. Kjellander, W.T. Smaal, J.E. Anthony, G.H. Gelinck, *Adv. Mater.* **2010**, *22*, 4612.
- [15] M.R. Niazi, R. Li, E. Qiang Li, A.R. Kirmani, M. Abdelsamie, Q. Wang, W. Pan, M.M. Payne, J.E. Anthony, D.M. Smilgies, S.T. Thoroddsen, E.P. Giannelis, A. Amassian, *Nat. Commun.* **2015**, *6*, 8598.
- [16] K. Zhao, O. Wodo, D. Ren, H.U. Khan, M.R. Niazi, H. Hu, M. Abdelsamie, R. Li, E.Q. Li, L. Yu, B. Yan, M.M. Payne, J. Smith, J.E. Anthony, T.D. Anthopoulos, S.T. Thoroddsen, B. Ganapathysubramanian, A. Amassian, *Adv. Funct. Mater.* **2016**, *26*, 1737.
- [17] X. Zhang, J. Jie, W. Deng, Q. Shang, J. Wang, H. Wang, X. Chen, X. Zhang, *Adv. Mater.* **2016**, *28*, 2475.
- [18] H. Sun, Q. Wang, J. Qian, Y. Yin, Y. Shi, Y. Li, *Semicond. Sci. Technol.* **2015**, *30*, 054001.
- [19] W. Deng, X. Zhang, H. Dong, J. Jie, X. Xu, J. Liu, L. He, L. Xu, W. Hu, X. Zhang, *Mater. Today* **2018**.
- [20] C.J. Brinker, in *Chemical solution deposition of functional oxide thin films*, (Eds: T. Schneller, R. Waser, M. Kosec, D. Payne), Springer, Vienna, Austria **2013**, pp. 233-261.

- [21] K. Wu, H. Li, L. Li, S. Zhang, X. Chen, Z. Xu, X. Zhang, W. Hu, L. Chi, X. Gao, Y. Meng, *Langmuir* **2016**, *32*, 6246.
- [22] T. Leydecker, D. Trong Duong, A. Salleo, E. Orgiu, P. Samori, *ACS Appl. Mater. Interfaces* **2014**, *6*, 21248.
- [23] G. Generali, F. Dinelli, R. Capelli, S. Toffanin, F. di Maria, M. Gazzano, G. Barbarella, M. Muccini, *J. Phys. Chem. C* **2011**, *115*, 23164.
- [24] Z.-T. Huang, C.-C. Fan, G.-B. Xue, J.-K. Wu, S. Liu, H.-B. Li, H.-Z. Chen, H.-Y. Li, *Chin. Chem. Lett.* **2016**, *27*, 523.
- [25] X. Gu, L. Shaw, K. Gu, M.F. Toney, Z. Bao, *Nat. Commun.* **2018**, *9*, 534.
- [26] R. Janneck, F. Vercesi, P. Heremans, J. Genoe, C. Rolin, *Adv. Mater.* **2016**, *28*, 8007.
- [27] K. Zhang, P. Wucher, T. Marszalek, M. Babics, A. Ringk, P.W.M. Blom, P.M. Beaujuge, W. Pisula, *Chem. Mater.* **2018**, *30*, 5032.
- [28] S. Kaya, P. Rajan, H. Dasari, D.C. Ingram, W. Jadwisienczak, F. Rahman, *ACS Appl. Mater. Interfaces* **2015**, *7*, 25024.
- [29] H. Bodiguel, F. Doumenc, B. Guerrier, *Langmuir* **2010**, *26*, 10758.
- [30] M.J. Large, S.P. Ogilvie, A.A.K. King, A.B. Dalton, *Langmuir* **2017**, *33*, 14766.
- [31] S. Feng, D. Ma, Y. Qiu, L. Duan, *RSC Adv.* **2018**, *8*, 4153.
- [32] K. Norrman, A. Ghanbari-Siahkali, N.B. Larsen, *Annu. Rep. Prog. Chem., Sect. C: Phys. Chem.* **2005**, *101*, 174.
- [33] J.Y. Oh, W.S. Jang, T.I. Lee, J.-M. Myoung, H.K. Baik, *Appl. Phys. Lett.* **2011**, *98*, 023303.
- [34] Q. Yang, J. Wang, X. Zhang, J. Zhang, Y. Fu, Z. Xie, *Sci. China: Chem.* **2014**, *58*, 309.
- [35] Z. Xu, L.-M. Chen, G. Yang, C.-H. Huang, J. Hou, Y. Wu, G. Li, C.-S. Hsu, Y. Yang, *Adv. Funct. Mater.* **2009**, *19*, 1227.
- [36] S. Kwon, J. Kim, G. Kim, K. Yu, Y.R. Jo, B.J. Kim, J. Kim, H. Kang, B. Park, K. Lee, *Adv. Mater.* **2015**, *27*, 6870.
- [37] M. Moret, M. Campione, A. Borghesi, L. Miozzo, A. Sassella, S. Trabattoni, B. Lotz, A. Thierry, *J. Mater. Chem.* **2005**, *15*, 2444.
- [38] J. Chen, M. Shao, K. Xiao, Z. He, D. Li, B.S. Lokitz, D.K. Hensley, S.M. Kilbey, J.E. Anthony, J.K. Keum, A.J. Rondinone, W.-Y. Lee, S. Hong, Z. Bao, *Chem. Mater.* **2013**, *25*, 4378.

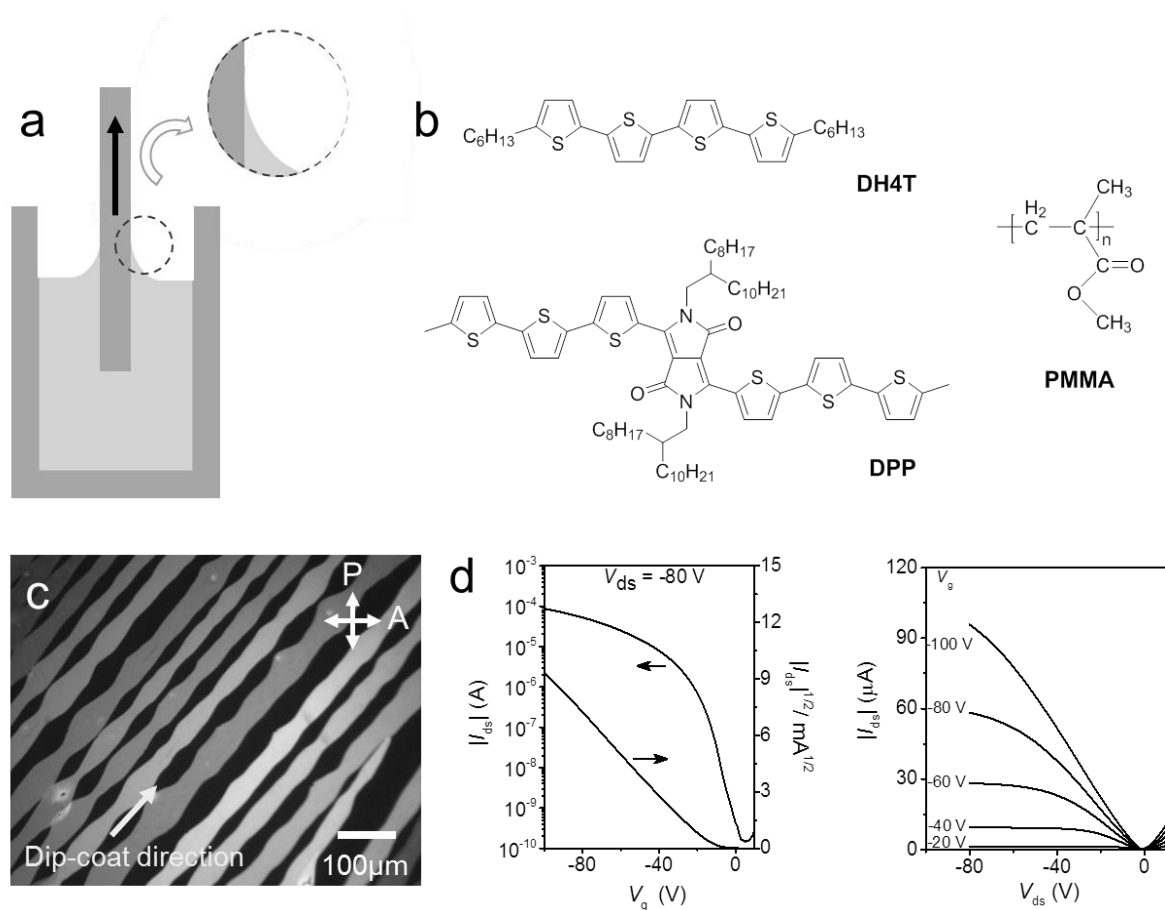


Figure 1. (a) Schematic illustration of the dip-coating process (inset: magnification of meniscus), (b) molecular structures of DH4T, DPP6T and PMMA, (c) POM image and (d) transfer and output characteristics of dip-coated DH4T:PMMA_(100 kDa, 10%) film.

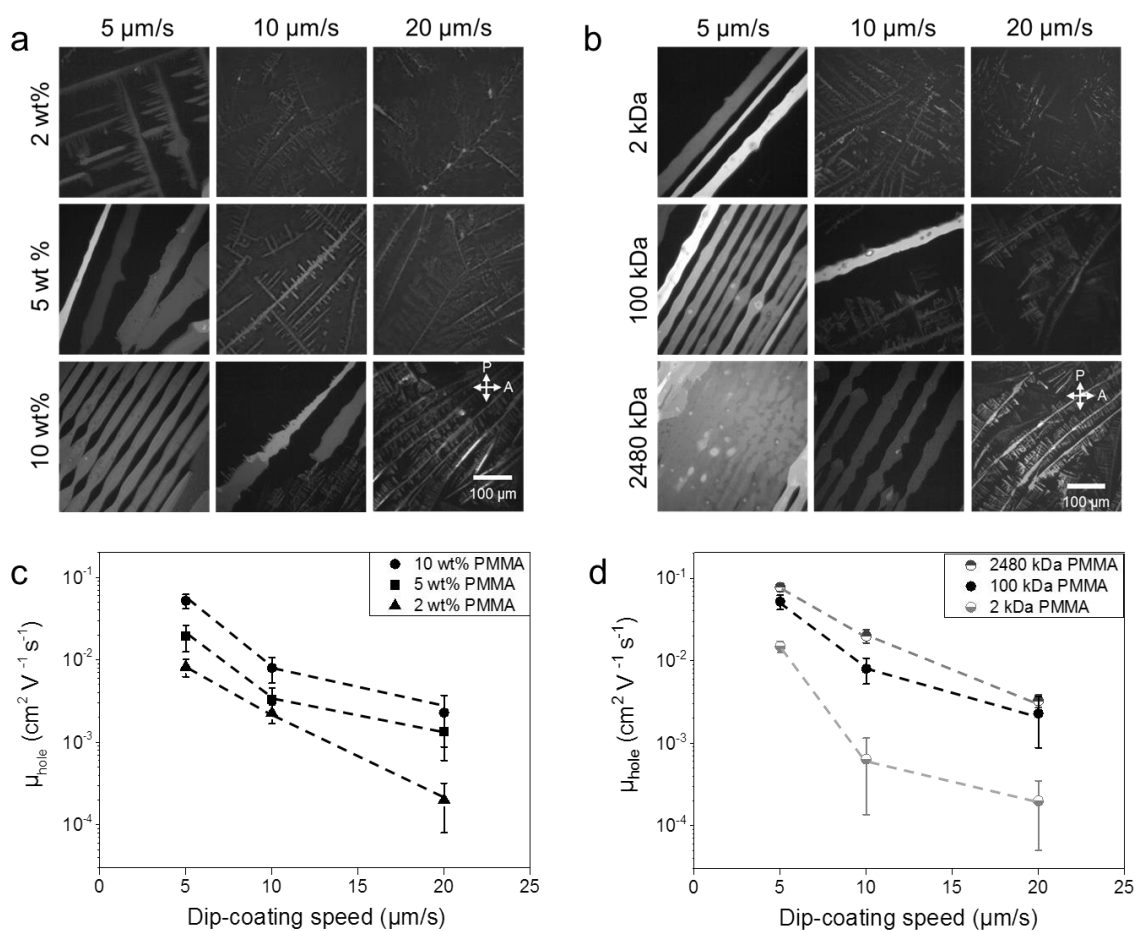


Figure 2. POM images and hole charge carrier mobility of dip-coated DH4T:PMMA films for various (a,c) weight fractions of PMMA (at 100 kDa) and (b,d) MWs of PMMA (at 10 wt%).

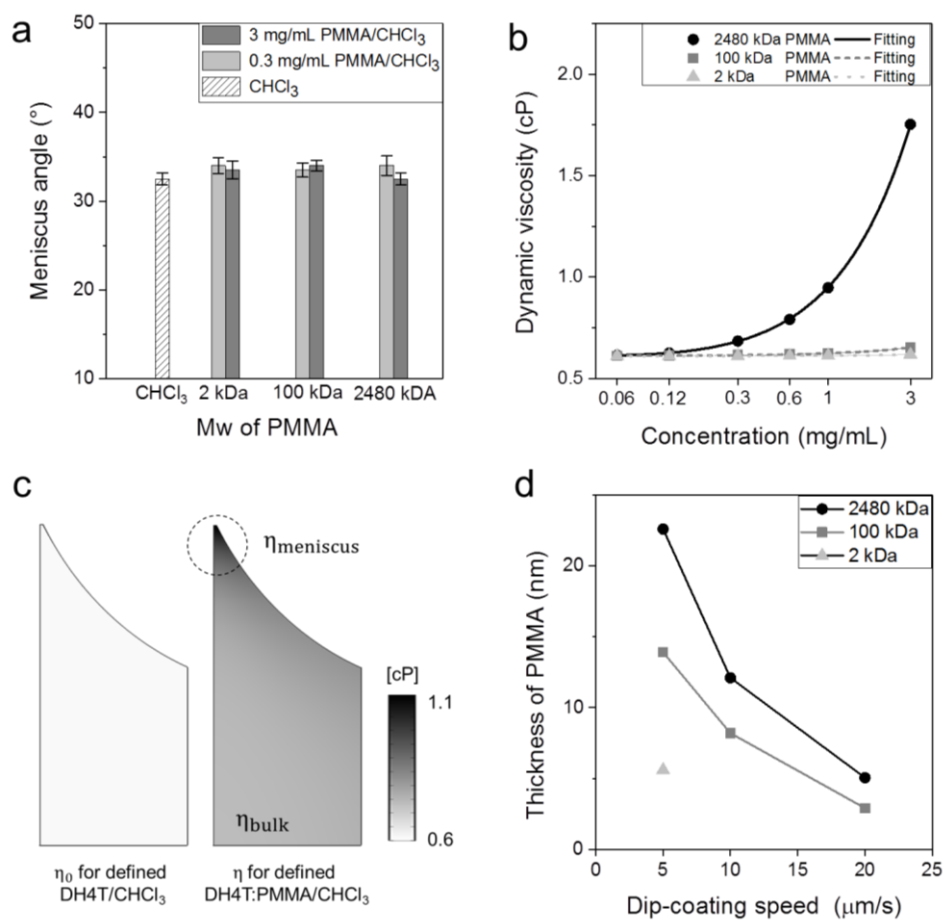


Figure 3. (a) Meniscus angle of PMMA/CHCl₃ solution during dip-coating, (b) dynamic viscosity of dilute PMMA/CHCl₃ bulk solution, (c) calculated dynamic viscosity at the meniscus of defined DH4T/CHCl₃ solution ($\eta_0 = 0.61$ cP) and defined DH4T:PMMA/CHCl₃ solution ($\eta_{\text{bulk}} = 0.68$ cP), (d) average thicknesses of dip-coated PMMA from 0.3mg/mL CHCl₃ obtained at different coating speed.

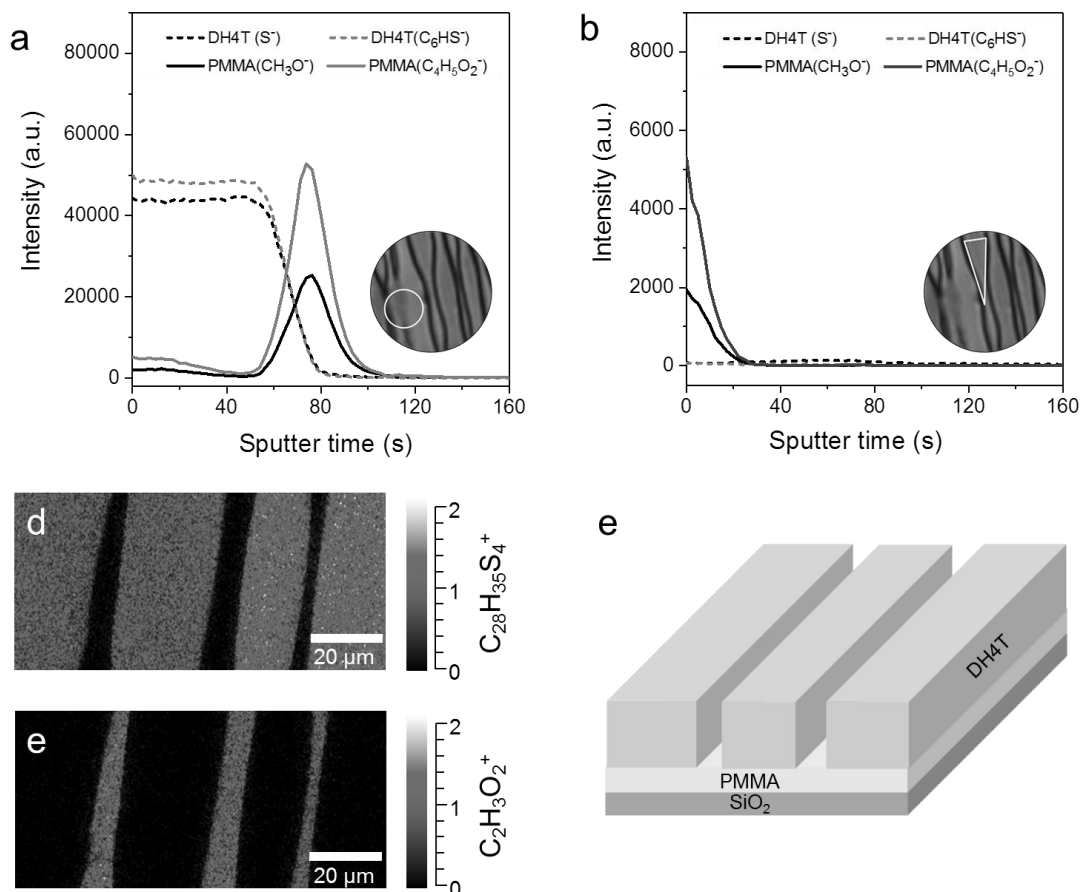


Figure 4. ToF-SIMS depth profiles of dip-coated DH4T:PMMA_(2480 kDa, 10%) films reconstructed from the areas indicated by (a) circles and (b) triangles, (c) and (d) lateral distributions of characteristic secondary ion signals on the top surface of dip-coated DH4T:PMMA films obtained by ToF-SIMS imaging analysis, (e) schematic cross-section diagram of the DH4T and PMMA distribution in the dip-coated films.

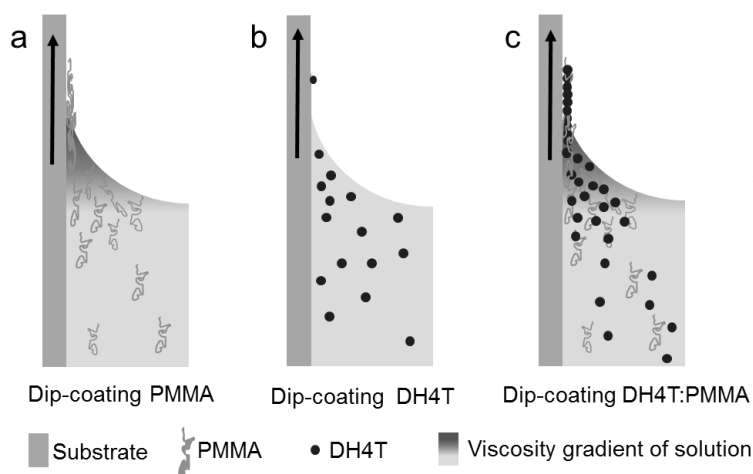


Figure 5. Schematic illustration for the dip-coating of (a) PMMA, (b) DH4T, and (c) DH4T:PMMA (with optimized wt% and MW of PMMA).

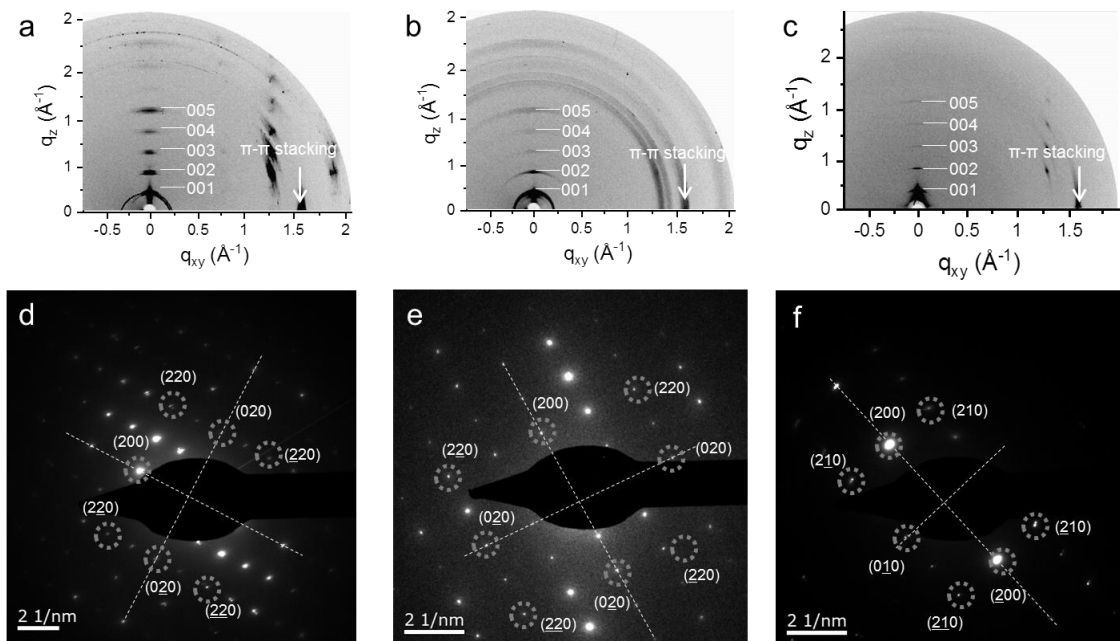


Figure 6. GIWAXS and SAED patterns of (a,d) drop-cast DH4T, (b,e) drop-cast and (c,f) dip-coated DH4T:PMMA_(2480 kDa, 10%). Miller indices are used to assign the reflections.

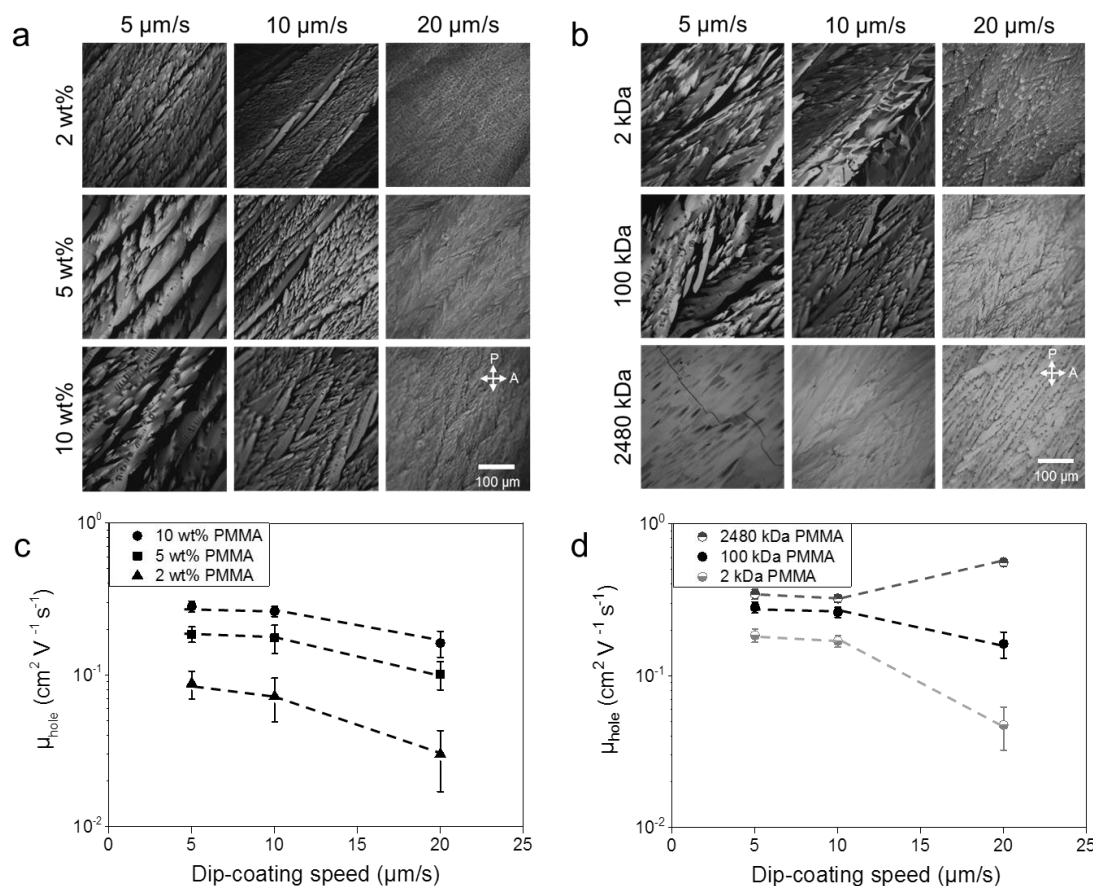


Figure 7. POM images and hole charge carrier mobility of dip-coated DPP6T:PMMA films for varying (a,c) the weight fraction of PMMA (100 kDa) and (b,d) MW of PMMA (10 wt%).

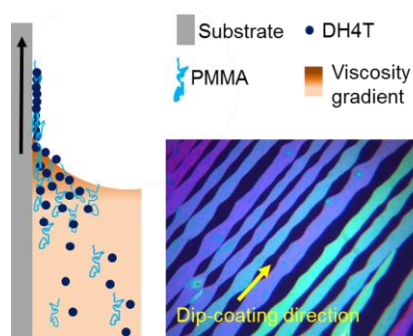
Table of Contents

Crystallization of small molecular organic semiconductors (OSCs) during meniscus-guided coating was enhanced by blending with a minor amount of an insulating polymer binder. The polymer binder increased mass transport and formed a bottom layer reducing the nucleation barrier height for OSC crystallization. The aligned crystalline films with stratified OSC/polymer layers contribute to a high charge transport in field effect transistors.

Keywords: dip-coating, semiconductor-insulator blend, crystallization control, morphology, organic field-effect transistor

Ke Zhang, Tomasz Marszalek, Philipp Wucher, Zuyuan Wang, Lothar Veith, Hao Lu, Hans-Joachim Räder, Pierre M. Beaujuge, Paul W. M. Blom, and Wojciech Pisula*

Crystallization Control of Organic Semiconductors during Meniscus-Guided Coating by Blending with Polymer Binder



Dip-coating DH4T:PMMA